Society For Biomaterials

Influence of nanoporosity on the nature of hydroxyapatite formed on bioactive calcium silicate model glass

Ukrit Thamma,[1] **Tia Kowal**,[2] **Matthias Falk**,[2] **Himanshu Jain**[1]

[1]Department of Materials Science and Engineering, Lehigh University, Bethlehem, 18015, Pennsylvania
[2]Department of Biological Sciences, Lehigh University, Bethlehem, 18015, Pennsylvania

Received 29 January 2018; revised 24 May 2018; accepted 28 May 2018
Published online 29 September 2018 in Wiley Online Library (wileyonlinelibrary.com). DOI: 10.1002/jbm.b.34184

Abstract: For hard tissue regeneration, the bioactivity of a material is measured by its ability to induce the formation of hydroxyapatite (HA) under physiological conditions. It depends on the dissolution behavior of the glass, which itself is determined by the composition and structure of glass. The enhanced HA growth on nanoporous than on nonporous glass has been attributed by some to greater specific surface area (SSA), but to nanopore size distribution by others. To decouple the influence of nanopore size and SSA on HA formation, we have successfully fabricated homogeneous 30CaO-70SiO_2 (30C70S) model bioactive glass monoliths with different nanopore sizes, yet similar SSA via a combination of sol–gel, solvent exchange, and sintering processes. After incubation in PBS, HA, and Type-B carbonated HA (HA/B-CHA) form on nanoporous monoliths. The XPS, FTIR, and SEM analyses provide the first unambiguous demonstration of the influence of nanopore size alone on the formation pathway, growth rate, and microstructure of HA/CHA. Due to pore-size limited diffusion of PO_4^{3-}, two HA/CHA formation pathways are observed: HA/CHA surface deposition and/or HA/CHA incorporation into nanopores. HA/CHA growth rate on the surface of a nanoporous glass monolith is dominated by the pore-size limited transport of Ca^{2+} ions dissolved from nanoporous glass substrates. Furthermore, with increasing nanopore size, HA/CHA microstructures evolve from needle-like, plate-like, to flower-like appearance. © 2018 Wiley Periodicals, Inc. J Biomed Mater Res Part B: Appl Biomater 107B: 886–899, 2019.

Key Words: bioactive glass, biomaterial, nanoporosity, hydroxyapatite formation, hydroxyapatite microstructure

How to cite this article: Thamma U, Kowal T, Falk M, Jain H. 2019. Influence of nanoporosity on the nature of hydroxyapatite formed on bioactive calcium silicate model glass. J Biomed Mater Res Part B 2019:107B:886–899.

INTRODUCTION

In the field of hard tissue regeneration, bioactivity of a material is measured by its ability to form hydroxyapatite (HA), $Ca_{10}(PO_4)_6(OH)_2$, under physiological conditions.[1] HA is a naturally occurring, inorganic mineral abundantly found in hard tissues, that is, bones and teeth. It possesses a hexagonal crystal structure, and due to the symmetry of unit cell, HA crystals preferably grow along the c-axis, naturally shaped as hexagonal rods.[2,3] With chemical and crystallographic properties similar to that of bones, HA layer formed on bioactive glasses has been shown to be critical for the biological interaction and bonding between glass substrate and osteoblast cells.[4]

In the past few decades, melt-quench 45S5 Bioglass® (46.1 mol % SiO_2, 26.9 mol % CaO, 4.5 mol % Na_2O, and 2.5 mol % P_2O_5), introduced in late 1960s by Hench,[1] has been studied widely because of its ability to readily form HA layer, leading to exceptional bone-bonding properties.[5] The superior bioactivity of 45S5 Bioglass® comes from the strategic compositional features with its relatively low content of silica (SiO_2) and high content of network modifiers Na_2O and CaO, leading to fast dissolution of silica and calcium ions previously shown to enhance cellular response.[6,7] Hench proposed a series of reactions that leads to the formation of HA on the surface of melt-quench 45S5 Bioglass® after immersion in physiological solution, that is, simulated body fluid (SBF), as follows[8]:

i. Rapid ion exchange reactions between glass network modifiers (Na^+ and Ca^{2+}) with H^+ or H_3O^+ from SBF solution. This results in the formation of silanol (Si—OH) groups on the glass surface and higher pH due to consumption of H^+ from the solution:

$$Si-O-Na + H^+ \rightarrow Si-OH + Na^+(aq) \qquad (1.1)$$

Correspondence to: H. Jain; e-mail: h.jain@lehigh.edu
Contract grant sponsor: National Science Foundation (PFI:AIR-TT); contract grant number: IIP-1602057
Contract grant sponsor: International Materials Institute for New Functionality in Glass; contract grant number: DMR-0844014

$$Si-O-Ca+2H^{+}\rightarrow Si-OH+Ca^{2+}(aq) \quad (1.2)$$

ii. Dissolution of SiO_2 network in the form of silicic acid ($Si(OH)_4$) and the continued formation of Si—OH on the glass surface:

$$Si-O-Si+H_2O\rightarrow Si-OH+HO-Si \quad (1.3)$$

iii. Condensation and repolymerization of amorphous SiO_2 on Na/Ca-depleted glass surface, creating amorphous SiO_2-rich layer.
iv. Formation of amorphous calcium phosphate (ACP) layer on SiO_2-rich film through the migration of soluble Ca^{2+} and $PO_3{}^{4-}$ from the continued dissolution of glass and pre-existing ions from SBF solution.
v. Formation of HA via further growth and crystallization of ACP layer.

Similar mechanism is expected for HA formation on sodium/calcium silicate glasses. Since the formation of HA is dependent on the concentration of Ca^{2+}, $PO_4{}^{3-}$, OH^{-}, and soluble species like $Si(OH)_4$, the characteristics of HA layer are governed by the dissolution behavior and the composition of the glass substrate. By introducing nanoporosity into the glass structure via the sol–gel process, the dissolution rate and HA growth rate on nanoporous sol–gel-derived glass are drastically enhanced compared to that of nonporous melt-quench glass substrate.[9] Whereas faster HA growth on nanoporous glass, compared to nonporous glass, was hypothesized to be associated with greater specific surface area (SSA),[10] a study by Peltola et al. argued that hydroxycarbonate apatite formation on porous sol–gel-derived SiO_2 and $CaO—P_2O_5—SiO_2$ substrates is enhanced by greater mesopore volume and wider mesopore size distribution, while minimally affected by the SSA of the underlying substrates.[11] Although empirical differences in HA formation behaviors between nonporous, melt-quench glass, and nanoporous sol–gel-derived glass have been presented in previous studies,[9,11] the effect of nanoporosity on the formation mechanism and characteristics of HA layer has remained unclear. In this article, we describe a series of experiments that decouple the influence of nanopore size and SSA on HA formation by investigating samples with different nanopore sizes yet similar SSA. To establish chemical pathways of HA formation unambiguously, we have selected a binary calcium silicate composition $30CaO—70SiO_2$ (30C70S) as the model system, which has shown strong potential as bioscaffolds for hard tissue regeneration.[11–14] In addition, we report direct evidence of the influence of nanopore size on HA formation and its microstructure that is also expected to influence its performance as a bioscaffold.

MATERIALS AND METHODS

The nanoporous bioactive glass samples of 30 mol % CaO - 70 mol % SiO_2 composition were fabricated via sol–gel process using the following chemical reagents: tetramethoxysilane, TMOS (99%, Acros Organics); calcium nitrate tetrahydrate, $Ca(NO_3)_2.4H_2O$ (Sigma Aldrich); acetic acid, CH_3COOH (Fisher Chemical); aqueous hydrofluoric acid, HF (Fisher Chemical); and ammonium hydroxide, NH_4OH (Fisher Chemical). The starting sol was prepared by mixing 20 mL of 0.05 N CH_3COOH (pH 3.0), 9 mL of TMOS, and 6.18 g of $Ca(NO_3)_2.4H_2O$. After adding HF to induce gelation, the sol was transferred and left to gel in closed Teflon jars at 40°C for 1 h. Depending on the desired nanopore size, gelled samples were either left to age at 40°C for 4 days or subjected to a solvent exchange with NH_4OH under hydrothermal conditions in Teflon-lined autoclave containers for 4 days at temperatures ranging from 120°C to 200°C. The aged gels were dried in open atmosphere at gradually increasing temperature at the heating rate of 5°C/min up to 180°C for 2 days. The dried gels were then thermally stabilized by heating at 2°C/min to 600°C and holding at this temperature for 5 h.

To obtain flat, uniform, monolithic samples nanoporous glass was ground and sieved to obtain glass powder with particle size <45 μm. The resulting powder was mixed, and then pressed into ~0.5-g disks with a uniaxial press in a cylindrical alumina die. To further strengthen and assure uniform green density, the pre-shaped disks were further pressed isostatically at 275 MPa. To achieve similar specific surface area (SSA) for different nanopore sizes, nanoporous glass disks were then sintered for 2 h in a Lindberg/Blue M three-zone tube furnace (Thermo Scientific, Waltham, MA) at various temperatures ranging from 600°C to 900°C. The pore size distribution and SSA of samples fabricated with different aging and sintering conditions were determined by nitrogen adsorption porosimetry (ASAP2020, Micrometrics, Norcross, GA).

To induce formation of hydroxyapatite (HA), autoclave-sterilized 30C70S nanoporous monoliths were immersed and incubated in phosphate-buffered saline (PBS) solution at 37°C, 5% CO_2–95% air, and saturated humidity for 3 days. The PBS solution is calcium-free, water-based salt solution containing 137 mM of sodium chloride (NaCl), 2.7 mM of potassium chloride (KCl), 10 mM of disodium hydrogen phosphate (Na_2HPO_4), and 1.8 mM of potassium dihydrogen phosphate (KH_2PO_4). Ionic concentrations, Ca^{2+} and $PO_4{}^{3-}$, and pH of the pre- and post-incubation PBS solutions were measured using Quantichrom assay kits (BioAssays Systems, Hayward, CA) and HI2210 pH meter (Hanna Instruments, Woonsocket, RI), respectively.

After incubation in PBS, nanoporous samples were rinsed with deionized water, and dried in ambient air. The chemical composition and crystallinity of PBS-incubated samples were determined by a Scienta ESCA 300 X-ray photoelectron spectroscopy (XPS) with monochromatic Al-K_α X-rays (1486.6 eV), and Panalytical Empyrean X-ray Diffractometer with a Cu X-ray tube (45 mA/40 kV) at a wavelength of 1.541Å, respectively. The binding energy scale of XPS spectra was referenced to C(1s) of adventitious carbon at 285.0 eV and the core levels of constituent elements were fitted with 70% Gaussian and 30% Lorentzian line shapes using CasaXPS data processing software.

The microstructure of the HA layer formed on each nanopore size during incubation in PBS was characterized using a

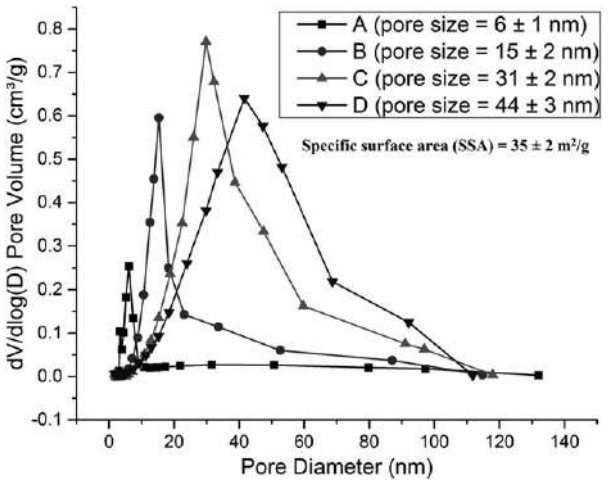

FIGURE 1. Pore size distribution of various nanopore sizes: A = 6-nm pore size, B = 15-nm pore size, C = 31- nm pore size, and D = 44-nm pore size, with similar specific surface area (SSA) of 35 ± 2 m^2/g.

Zeiss 1550 scanning electron microscope (SEM). To quantify the thickness of HA layer, elemental maps of the cross-sections from PBS-incubated samples were obtained by energy dispersive spectroscopy (EDS). To further determine the molecular structure of HA layer, attenuated total reflection Fourier transform infrared (ATR-FTIR) spectra from PBS-incubated samples were acquired using a Bruker Vertex 70 spectrometer (Bruker Optics, Billerica, MA) equipped with a MVP Pro single reflection diamond crystal ATR accessory (Harrick Scientific, Pleasantville, NY). These spectra were acquired using a mercury cadmium telluride (MCT) detector in the mid-infrared range of 650 cm^{-1} to 4000 cm^{-1} wavenumber by averaging 400 scans at 6 cm^{-1} resolution and were reported in absorbance units by referencing to the spectrum of the bare ATR crystal.

RESULTS

Pore sizes and specific surface area of nanoporous glass monoliths

The pore size distribution and SSA of samples fabricated with different aging and sintering conditions are summarized in Figure 1 and Table I, respectively. The selected nanopore sizes of samples with similar specific surface area were 6 ± 1 nm, 15 ± 2 nm, 31 ± 2 nm, and 44 ± 3 nm with SSA of 35 ± 2 m^2/g.

XPS analysis of PBS-incubated nanoporous glass monoliths

A representative XPS spectrum of a PBS-incubated nanoporous glass monolith shows the presence of O, Ca, P, Na, Cl, F, and Ca on its surface, as shown in Figure 2. Here Na, Cl, and P came from PBS solution, and the presence of F is from the use of HF as a gelation catalyst in sol–gel process. Silicon, the main component of the underlying nanoporous glass, was not detected by XPS on PBS-incubated samples. Since the presence of carbon (C) is in the form of adventitious hydrocarbon contamination caused by the exposure of samples to ambient air prior to the XPS analysis, the peak positions were referenced and calibrated to the C(1s) binding energy of C—C/C—H at 285.0 eV.[15] Chemical composition of the layer formed on the surface of different nanopore size samples after 3-day PBS incubation is reported in Table II.

The representative deconvoluted C(1s), Na(1s), F(1s), Cl(2p), O(1s), Ca(2p), and P(2p) core level spectra of a PBS-incubated sample are shown in Figure 3(a–g), respectively. The core level binding energy with corresponding compounds based on values in the literature, and average content in mol % present on PBS-incubated samples with are summarized in Table III for 30C70S samples with different nanopore sizes. The deconvoluted C(1s) spectrum in Figure 3(a) depict three distinct peaks located at 285 ± 0.0 eV (used as the binding energy reference), 286.1 ± 0.1 eV, and 289.4 ± 0.1 eV, which correspond to the binding energies of C(1s) in C—C/C—H,[15] C—O,[16] and O—C═O[17] molecular units, respectively. The C—C/C—H and C—O peaks are due to hydrocarbon contamination, and the O—C═O peak indicates the presence of carbonate groups. The area under the peak of each carbon species in the deconvoluted C (1s) core spectra yielded the concentrations of various carbon species as 5.2 ± 0.5 mol % in the form of C—C/C—H, 1.2 ± 0.5 mol % in the form of C—O, and 1.2 ± 0.2 mol % in the form of O—C═O (carbonate groups).

The Na(1s) spectrum in Figure 3(b) depicts a single peak at 1072.0 ± 0.1 eV, which corresponds to the binding energy of Na in NaH_2PO_4.[18] The deconvoluted F(1s) spectrum in Figure 3(c) also shows a single peak at 684.8 ± 0.1 eV, which agrees with the binding energy of F in CaF_2.[19] The deconvoluted Cl(2p) spectra in Figure 3(d) exhibits two distinct peaks at 200.5 ± 0.1 eV and 199.0 ± 0.1 eV, which are assigned to Cl($2p_{1/2}$) and Cl($2p_{3/2}$), respectively. The main Cl($2p_{3/2}$) binding energy peak at 199.0 eV corresponds to the Cl in $CaCl_2$.[20] It is worth noting that, although Na^+ ions in PBS solution can compete with Ca^{2+} ions to form NaF and

TABLE I. Summary of Aging and Sintering Conditions During Sol–Gel Process Leading to Various Nanopore Sizes with Similar Specific Surface Area

			Aging Condition		
Sample	Pore Size	Surface Area	Solvent Exchange	Temperature (°C)	Sintering Temperature (°C)
A	6 ± 1 nm	36 ± 1 m^2/g	None	40	775
B	15 ± 2 nm	35 ± 2 m^2/g	1 M NH_4OH	120	755
C	31 ± 2 nm	35 ± 1 m^2/g	1 M NH_4OH	180	740
D	44 ± 3 nm	37 ± 1 m^2/g	1 M NH_4OH	200	None

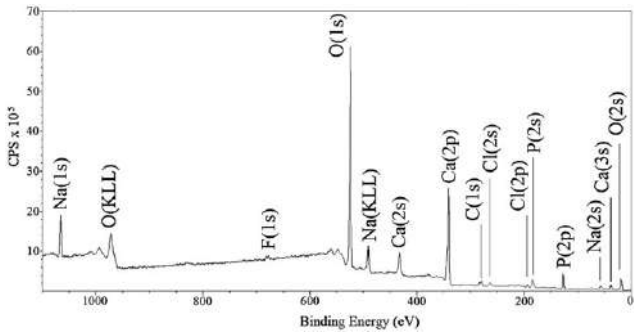

FIGURE 2. Representative XPS spectrum of a PBS-incubated nanoporous glass monolith.

NaCl, the Gibbs free energy of formation (ΔG_f) of CaF_2 (−1111 kJ/mol) and $CaCl_2$ (−816 kJ/mol) are lower than ΔG_f values of NaF (−541 kJ/mol) and NaCl (−393 kJ/mol),[21] thus, favoring the formation of CaF_2 and $CaCl_2$ as suggested by XPS analysis.

The deconvoluted O(1s) spectrum in Figure 3(e) depicts two distinct peaks located at 532.2 ± 0.1 eV and 531.4 ± 0.1 eV. The O(1s) peak at 532.2 eV agrees with the binding energy of O(1s) of NaH_2PO_4.[18] The O(1s) peak at 531.4 eV is in agreement with the O(1s) binding energy of hydroxyapatite or HA ($Ca_{10}(PO_4)_6(OH)_2$)[22] and carbonated hydroxyapatite or CHA,[17] which can be either Type-A CHA, wherein CO_3^{2-} substitutes for OH^- yielding ($Ca_{10}(PO_4)_6(CO_3)_x(OH)_{2-2x}$),[23,24] or Type-B CHA, wherein CO_3^{2-} substitutes for PO_4^{3-} yielding ($Ca_{10}(PO_4)_{6-[2x/3]}(CO_3)_x(OH)_2$).[25,26] Since the binding energy of Na(1s) at 1072.0 eV obtained from the XPS spectra of PBS-incubated samples does not correspond to the presence of Na_2CO_3 with Na(1s) binding energy of 1071.5 eV,[27] it can be assumed that all carbonate groups are incorporated in CHA. By balancing the content of detected elements, CHA found in this work is derived to be Type B with the chemical formula of ($Ca_{10}(PO_4)_2(CO_3)_6(OH)_2$). The average molar ratio of HCA to HA is approximately 0.19 ± 0.03. By analyzing the area under the peak of each oxygen species in the deconvoluted O (1s) core spectra, there are 13.6 ± 0.9 mol % of oxygen in NaH_2PO_4 and 36.7 ± 1.0 mol % of oxygen in HA/CHA form.

The deconvoluted Ca(2p) spectrum in Figure 3(f) depicts two distinct peaks at 347.7 ± 0.1 eV and 351.3 eV ± 0.1 eV, representing Ca($2p_{3/2}$) and Ca($2p_{1/2}$), respectively. The binding energy of Ca($2p_{3/2}$) at 347.7 eV is comparable to that of Ca in CaF_2,[19] $CaCl_2$,[20] HA ($Ca_{10}(PO_4)_6(OH)_2$),[21] and Type-B CHA ($Ca_{10}(PO_4)_2(CO_3)_6(OH)_2$).[17] The deconvoluted P (2p) spectrum in Figure 3(g) shows two distinct peaks at 133.9 eV ± 0.1 eV and 134.9 ± 0.1 eV which are assigned to P ($2p_{3/2}$) and P($2p_{1/2}$), respectively. The binding energy of P ($2p_{3/2}$) at 133.9 eV corresponds to the P in HA ($Ca_{10}(PO_4)_6(OH)_2$),[22] Type-B CHA ($Ca_{10}(PO_4)_2(CO_3)_6(OH)_2$),[17] and NaH_2PO_4.[18]

Based on the deconvolution of measured core spectra, five chemical compounds besides adventitious hydrocarbon, appear to be present on the surface of nanoporous samples after 3-day PBS incubation: NaH_2PO_4, CaF_2, $CaCl_2$, HA ($Ca_{10}(PO_4)_6(OH)_2$), and CHA ($Ca_{10}(PO_4)_2(CO_3)_6(OH)_2$). The XPS binding energies derived from the deconvolution of the core spectra of detected elements were indistinguishable for the HA layers formed on various 30C70S monoliths with different nanopore sizes, indicating that they consist of the same chemical compounds.

ATR-FTIR analysis of PBS-incubated nanoporous glass monoliths

To further identify the molecular structure of HA, ATR-FTIR spectroscopy was performed on PBS-incubated samples with different nanopore sizes. ATR-FTIR spectra of HA layer formed on 6-, 15-, 31-, and 44-nm are shown in Figure 4(a–d), respectively. Six characteristic absorbance peaks are observed for samples of all nanopore sizes: 3295 ± 15 cm^{-1}, 1637 ± 5 cm^{-1}, 1463 ± 5 cm^{-1}, 1418 ± 5 cm^{-1},1008 ± 7 cm^{-1}, and 869 ± 4 cm^{-1}. The absorbance peaks at 3295 cm^{-1} and 1637 cm^{-1} are attributed to the stretching and the bending vibrations of OH groups, respectively, in HA/CHA and adsorbed water residue.[28,29] The absorbance peak at 1016 cm^{-1} corresponds to the antisymmetric stretching vibration (v_3) of PO_4^{3-} molecules in HA/CHA and NaH_2PO_4.[30] The absorbance peaks at 1463 cm^{-1} and 1418 cm^{-1} are attributed to asymmetric stretching vibration (v_3) of CO_3^{2-}, whereas the absorbance peak at 869 cm^{-1} is attributed to the bending mode (v_2) of CO_3^{-2}.[31]

CO_3^{2-} molecules present in CHA can either substitute OH^- sites (Type-A CHA) or PO_4^{3-} sites (Type-B CHA), as previously discussed in XPS analysis of PBS-incubated nanoporous glass monoliths section. The positions of $v_3(CO_3^{2-})$ peaks can be shifted relative to HA, depending on which sites CO_3^{2-} substitutes in the apatite lattice.[32] The $v_3(CO_3^{2-})$ peaks of Type-A CHA were previously reported at 1546 cm^{-1} and 1465 cm^{-1}, and those of Type-B CHA were shown to be at 1465 cm^{-1} and 1413 cm^{-1}.[33] Whereas $v_3(CO_3^{2-})$ in both types of CHA has a common position at 1465 cm^{-1}, the v_3 peaks at 1546 cm^{-1} and 1413 cm^{-1} are characteristic of Type-A CHA and Type-B CHA, respectively. Since ATR-FTIR

TABLE II. Composition of Hydroxyapatite (HA) Layer Formed on Different Nanopore Sizes with Similar Specific Surface Area by XPS Analysis

	Composition in mol %						
Sample	O	Ca	P	Na	F	Cl	C
6-nm pore size	50.8 ± 5.1	17.9 ± 1.8	11.1 ± 1.1	3.6 ± 0.4	7.1 ± 0.7	1.9 ± 0.2	7.6 ± 0.8
15-nm pore size	51.8 ± 5.2	18.2 ± 1.8	11.5 ± 1.2	3.4 ± 0.3	6.8 ± 0.7	1.2 ± 0.1	7.1 ± 0.7
31-nm pore size	51.5 ± 5.2	18.1 ± 1.8	11.2 ± 1.1	3.5 ± 0.4	7.0 ± 0.7	1.4 ± 0.1	7.3 ± 0.7
44-nm pore size	51.3 ± 5.1	18.4 ± 1.9	11.1 ± 1.1	3.1 ± 0.3	6.9 ± 0.7	1.5 ± 0.2	7.7 ± 0.8

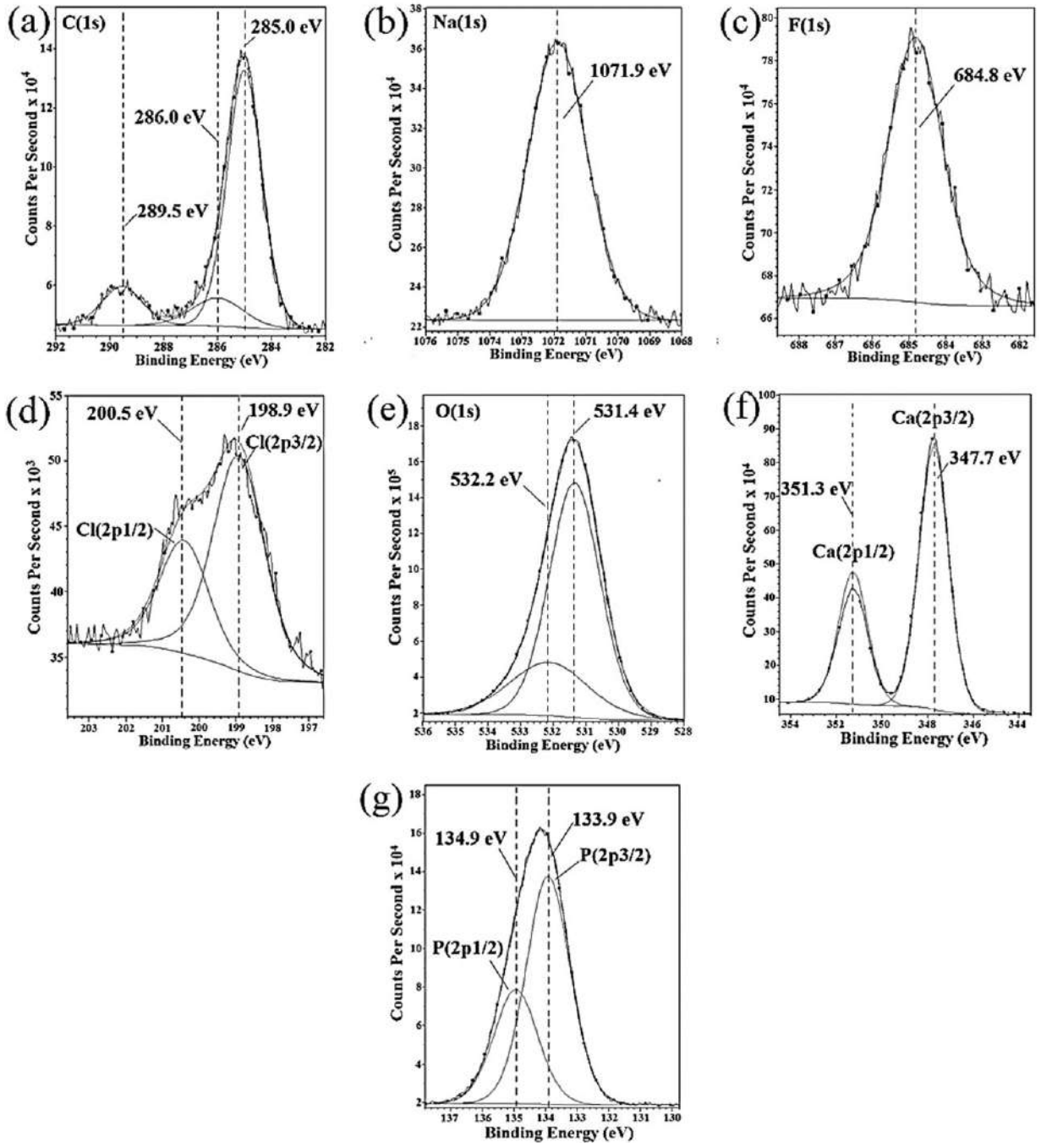

FIGURE 3. Representative core-level XPS spectra of a PBS-incubated 30C70S nanoporous glass monolith (a) C(1s), (b) Na(1s), (c) F(1s), (d) Cl(2p), (e) O(1s), (f) Ca(2p), and (g) P(2p).

spectra of all PBS-incubated samples depict strong v_3 absorbance of CO_3^{2-} at 1465 cm^{-2} and 1418 cm^{-1}, we establish the presence of Type-B CHA primarily on PBS-incubated nanoporous glass monoliths.

XRD analysis of PBS-incubated nanoporous glass monoliths

The XRD patterns of HA/CHA formed after 3-day PBS incubation on 6-, 15-, 31-, and 44-nm pore sizes are shown in Figure 5(a–d), respectively. The patterns show five main peaks at the diffraction angles 2θ = 25.9°, 31.8°, 32.9°, 49.5°, and 53.1°, which correspond to (002), (211), (300), (213), and (004) reflection planes of stoichiometric hydroxyapatite standard from the Joint Committee on Powder Diffraction Standards (JCPDS) data base, card number 09-0432[34] [-Figure 5(e)]. Since the XRD patterns of CHA and HA are indistinguishable due to its resemblance in both crystal structure and lattice parameters,[36] it is not possible to separate HA and CHA from the XRD patterns, but we simply confirm the predominance of HA/CHA deduced from XPS

TABLE III. Summary of the Binding Energy and the Corresponding Peak Assignment of Detected Elements at its Core Level for PBS-Incubated Samples with Different Nanopore Sizes

	Binding Energy (eV)					
Core Level	6 nm	15 nm	31 nm	44 nm	Average Content (mol %)	Peak Assignment
C(1s)	285.0	285.0	285.0	285.0	5.2 ± 0.5	C-C/C-H[15]
	286.0	286.0	286.0	286.2	1.2 ± 0.5	C-O[16]
	289.5	289.5	289.3	289.4	1.2 ± 0.2	O-C=O[17]
Na(1s)	1071.9	1071.9	1072.0	1072.0	3.5 ± 0.1	NaH_2PO_4[18]
F(1s)	684.8	684.9	684.8	684.8	7.0 ± 0.1	CaF_2[19]
Cl(2p3/2)	198.9	199.0	199.0	199.0	1.5 ± 0.3	$CaCl_2$[20]
O(1s)	531.4	531.4	531.4	531.5	36.7 ± 1.0	$HA(Ca_{10}(PO_4)_6(OH)_2)$[21] Type-B CHA $(Ca_{10}(PO_4)_2(CO_3)_6(OH)_2)$[17]
	532.2	532.1	532.1	532.2	13.6 ± 0.9	NaH_2PO_4[18]
Ca(2p3/2)	347.7	347.7	347.5	347.8	18.2 ± 0.2	CaF_2[19] $CaCl_2$[20] $HA(Ca_{10}(PO_4)_6(OH)_2)$[21] Type-B CHA $(Ca_{10}(PO_4)_2(CO_3)_6(OH)_2)$[17]
P(2p3/2)	133.9	133.8	133.8	133.9	11.2 ± 0.2	NaH_2PO_4[18] $HA(Ca_{10}(PO_4)_6(OH)_2)$[21] Type-B CHA $(Ca_{10}(PO_4)_2(CO_3)_6(OH)_2)$[17]

compositional analysis. In addition to the main peaks, there are two minor peaks in the XRD patterns at 2θ = 28.0° and 29.2°, which correspond to (121)-plane reflections of NaH_2PO_4 and (111)-plane reflections $CaF_2/CaCl_2$, respectively. The XRD reference patterns of CaF_2, $CaCl_2$, and $NaH_2PO_4.H_2O$ were obtained from International Center for Diffraction Data (ICDD) with Powder Diffraction File (PDF) number as follows: PDF-00-004-0864 [Figure 5(f)],[35] PDF-00-024-0223 [Figure 5(g)],[35] and PDF-00-011-0651 [Figure 5 (h)],[35] respectively.

The size of HA/CHA crystallites ($t_{(hkl)}$) was calculated by peak broadening analysis using the Scherrer equation[37,38]:

$$t_{(hkl)} = \frac{0.9\lambda}{B\cos\theta_{(hkl)}}$$

where λ is the wavelength of the monochromatic X-ray beam (1.541Å), B is the full width at half maximum (FWHM) in radians, $\theta_{(hkl)}$ is the location of the (hkl) peak. By using the (002) diffraction peaks at $2\theta_{(002)}$ = 25.9°, HA/CHA crystallite sizes formed on 6-, 15-, 31-, and 44-nm samples were 0.37 nm, 0.93 nm, 1.11 nm, and 0.56 nm, respectively.

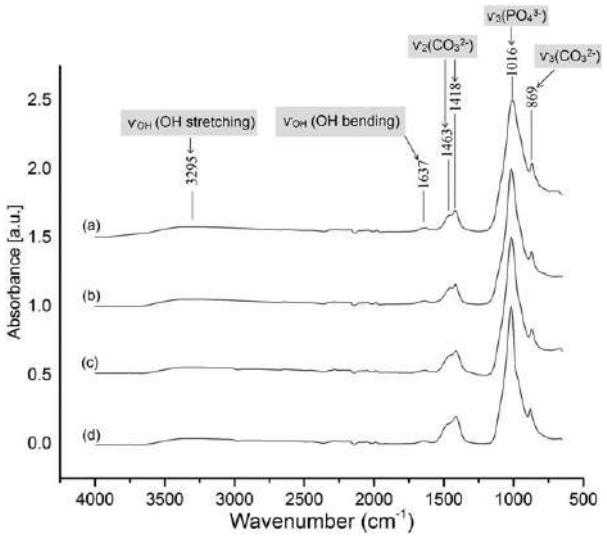

FIGURE 4. ATR FTIR spectra of PBS-incubated nanoporous glass monoliths with (a) 6-nm, (b) 15-nm, (c) 31-nm, and (d) 44-nm nanopore sizes.

Thickness and microstructure of PBS-incubated nanoporous glass monoliths

Cross-sectional backscattered electron (BSE) micrographs and corresponding EDS elemental maps for Ca, P, and Si of PBS-incubated nanoporous glass monoliths are shown in Figure 6. Due to its higher molar mass, HA/CHA layers in BSE micrographs appear as a relatively brighter region compared to the underlying nanoporous glass substrate. HA/CHA layer is identified by the coexistence of Ca and P signals in the same region in EDS elemental maps, and the nanoporous glass substrate is recognized by strong Si signal. The contiguous coverage of surface by HA/CHA layer is clearly seen in these micrographs.

For 6-, 15-, and 31-nm pore size samples, there is no overlap of HA/CHA layer (Ca and P) and Si in EDS elemental maps, indicating that HA/CHA was formed only on the surface of nanoporous glass substrates. In contrast, for 44-nm pore size sample, there are two different HA/CHA layers: "Pure HA/CHA" where HA/CHA formed on the surface of glass substrates and "HA/CHA + Glass" where HA/CHA was incorporated into the nanopores of glass substrates. The "Pure HA/CHA" layer with an overlap of only Ca and P is approximately 0.7 μm thick, whereas "HA/CHA + Glass" layer with an overlap of Ca, P, and Si is approximately 3.0 μm

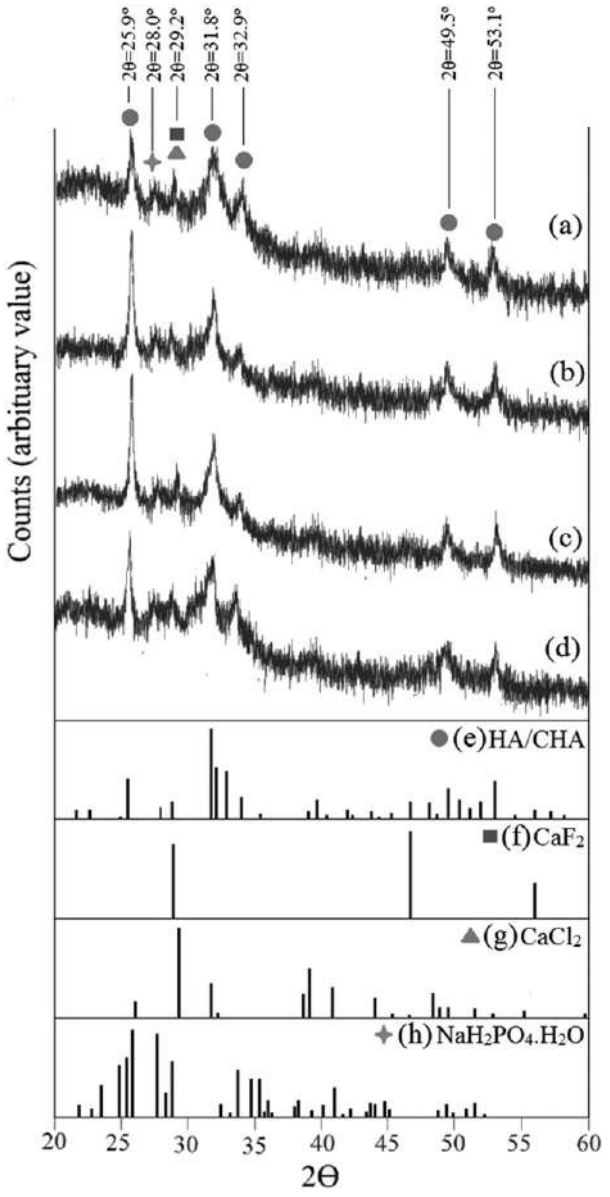

FIGURE 5. X-ray diffraction (XRD) patterns of HA/CHA formed on: (a) 6-nm pore size, (b) 15-nm pore size, (c) 31-nm pore size, and (d) 44-nm pore size, accompanied by XRD reference patterns of (e) hydroxyapatite (HA) (JCPDS #09–0432),[34] (f) CaF2 (ICDD-PDF#00–004-0864),[35] (g) CaCl2 (ICDD-PDF#00–024-0223),[35] and (h) NaH2PO4.H2O(ICDD-PDF#00–011-0651).[35]

thick. The thickness of HA/CHA layer formed on the surface of nanoporous glass monoliths with 6-, 15-, 31-, and 44-nm pore sizes are 1.5 μm, 2.1 μm, 2.7 μm, and 0.7 μm, respectively. The overall growth rate of HA/CHA layer over the PBS-incubation period can be ranked according to its thickness on the surface, excluding the thickness of "HA/CHA + Glass" layer formed by HA/CHA incorporation into the nanopores as seen in 44-nm samples. This average growth rate of surface-deposited HA layer on 6-, 15-, 31-, and 44-nm samples is 0.5 ± 0.1 μm/day, 0.7 ± 0.2 μm/day, 0.9 ± 0.2 μm/day, and 0.2 ± 0.1 μm/day, respectively. Therefore, nanopore sizes that provide the slowest to the fastest overall growth rate of HA are on 44-, 6-, 15-, and 31-nm samples.

Four distinct microstructures of HA/CHA layer on the surfaces of samples with different nanopore sizes were observed by SEM as shown in Figure 7. Specifically, microstructures appearing as long needles (LN), plates (PL), flowers (FW), and short needles (SN) were found on the surface of PBS-incubated samples with 6-, 15-, 31-, and 44- pore sizes, as seen in Figure 7(a–d), respectively. As the overall growth rate increases, HA/CHA microstructure evolves from short-needle, to long-needle, to plate-like, and then to flower-like appearance.

Ion concentration and pH of PBS solution before and after incubation

Since the dissolution behavior of glass is critical to HA/CHA formation, pH and the concentrations of calcium (Ca^{2+}) and phosphate (PO_4^{3-}) ions in PBS were measured before and after exposure to glass monoliths with different nanopore sizes as described in Figure 8. Calcium, which is not a part of initial PBS, was detected in PBS after exposure to nanoporous glasses along with higher pH. Conversely, phosphate concentrations in the post-incubation PBS were lower compared to the initial PBS.

Both pH and calcium concentration in the post-incubation PBS rise as the size of nanopores increases; however, phosphate concentration after exposure to nanoporous glasses decreases with increasing nanopore size. The pH of PBS solutions after 3-day incubation of nanoporous samples, shown in Figure 8(a), was 8.64 ± 0.04, 8.67 ± 0.05, 8.72 ± 0.06, and8.77 ± 0.05 for the 6-, 15-, 31-, and 44-nm nanoporous samples, respectively, which is higher than the pH of the pre-incubation PBS at 7.46 ± 0.05. While the pre-incubation PBS was calcium-free, calcium concentration in post-incubation PBS for samples with 6-, 15-, 31-, and 44-nm pore sizes was 3.7 ± 0.8 mM, 7.3 ± 1.3 mM, 15.2 ± 1.9 mM, and 18.4 ± 1.3 mM, respectively [see Figure 8(b)]. Phosphate concentration in post-incubation PBS for samples with 6-, 15-, 31-, and 44-nm pore sizes, shown in Figure 8 (c), was 7.3 ± 0.5 mM, 6.1 ± 0.4 mM, 3.8 ± 0.3 mM, and 2.7 ± 0.3 mM, respectively, all of which were less than the pre-incubation phosphate concentration of 8.5 ± 0.3 mM. Since all nanopore sizes possess similar SSA, these results suggest that diffusion of dissolved Ca^{2+}, a consequence of ion exchange and dissolution reactions of nanoporous glass substrate, and the removal of phosphate ions from PBS due to HA/CHA formation are determined by the size of nanopores.

DISCUSSION

Chemistry of hydroxyapatite formed on nanoporous 30C70S samples

As mentioned in the Introduction, reaction of calcium silicate glass with body fluids or PBS solution produces a layer of hydroxyapatite (HA) of standard composition, $Ca_{10}(PO_4)_6(OH)_2$, or its variant, carbonated hydroxyapatite (CHA). The later may be formed such that CO_3^{2-} ions substitutes for OH^- ions, yielding $(Ca_{10}(PO_4)_6(CO_3)_x(OH)_{2-2x})$ (Type-A CHA), or for PO_4^{3-} ions, yielding $(Ca_{10}(PO_4)_{6-[2x/3]}(CO_3)_x(OH)_2)$

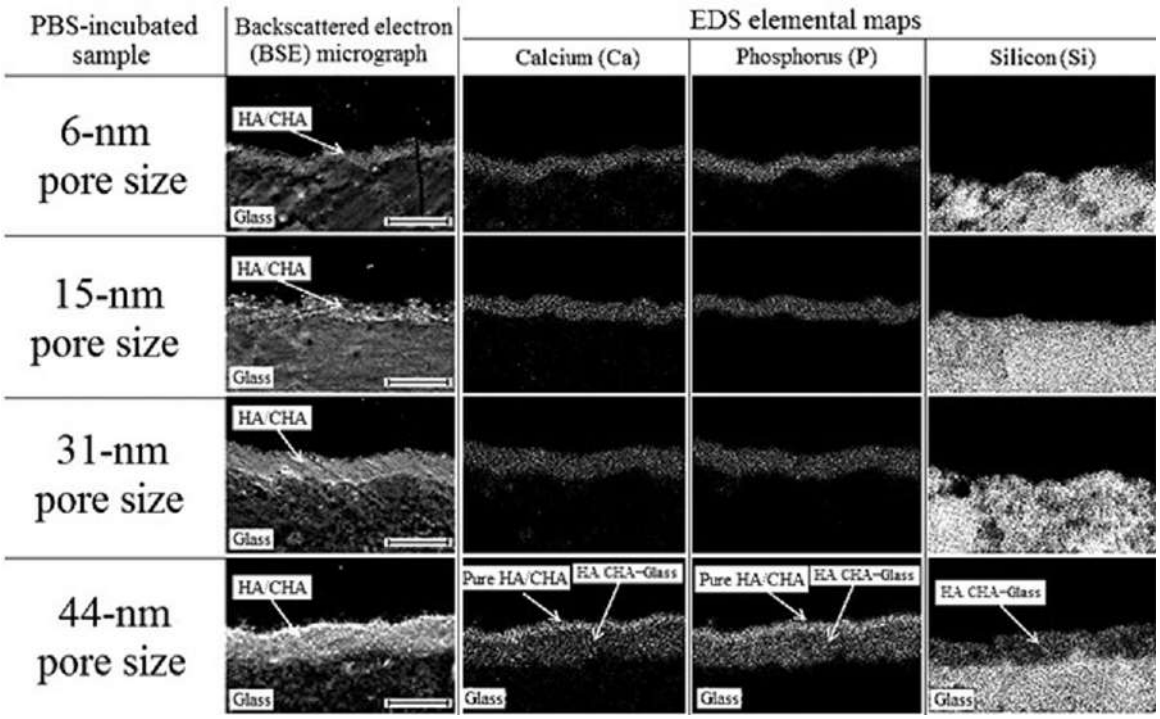

FIGURE 6. Cross-sectioned PBS-incubated nanoporous monoliths presented by backscattered electron (BSE) micrographs and its corresponding EDS elemental maps for Ca, P, and Si (scale bar = 5 μm).

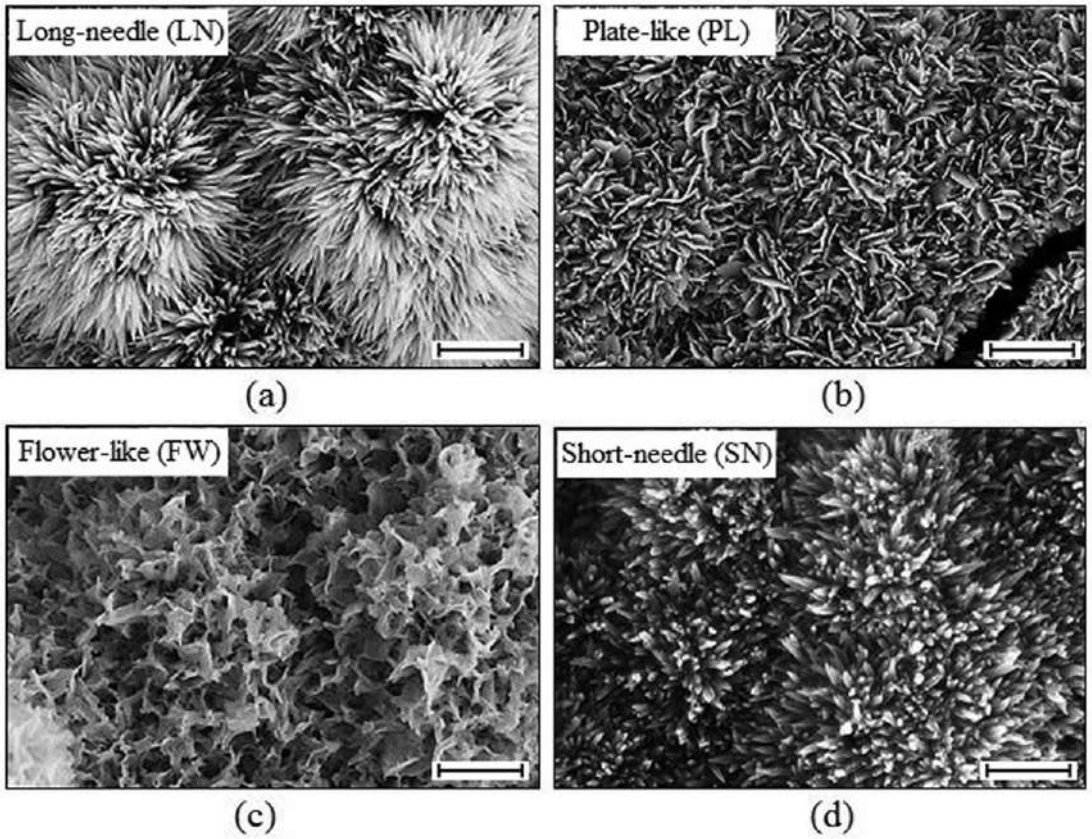

FIGURE 7. SEM micrographs of HA/CHA layer formed on nanoporous glass monoliths with (a) 6-nm (b) 15-nm, (c) 31-nm, and (d) 44-nm pore size and SSA of 36 m^2/g, yielding long-needle (LN), plate-like (PL), flowerlike (FW), and short-needle (SN), respectively (scale bar = 1 μm).

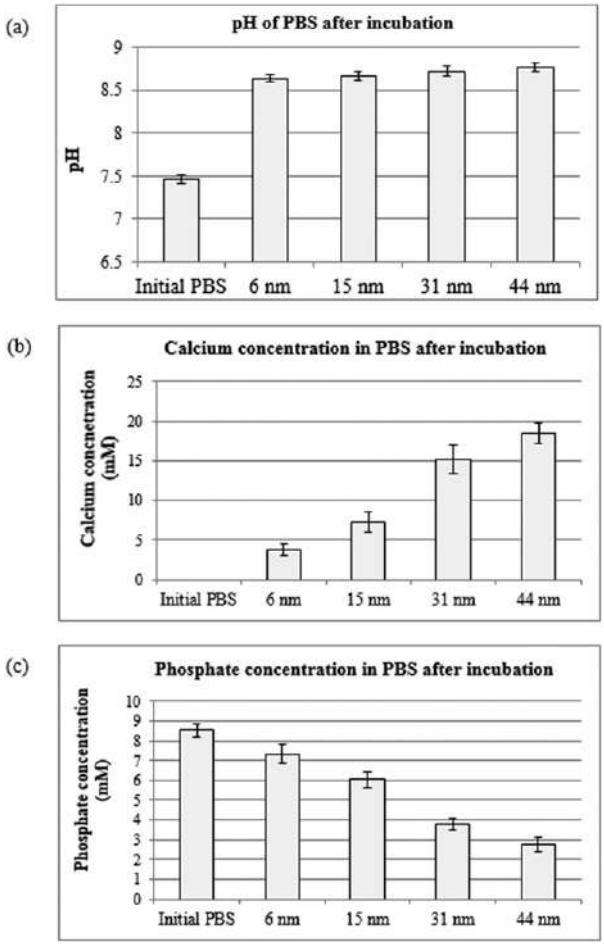

FIGURE 8. PBS conditions before and after incubation of nanoporous glass monoliths with different nanopore sizes and similar specific surface area: (a) pH (b) calcium concentration (c) phosphate concentration.

(Type-B CHA). We determined the kind of HA/CHA formed on 30C70S nanoporous glass monoliths after immersion in PBS by XPS and XRD as described in sections XPS analysis of PBS-incubated nanoporous glass monoliths and XRD analysis of PBS-incubated nanoporous glass monoliths, respectively. The type and chemical formula of the newly formed surface layer were deduced to be Type-B CHA [i.e., $Ca_{10}(PO_4)_2(CO_3)_6(OH)_2$] by balancing the atomic concentration of each element detected by XPS, with the assumption that all CO_3^{2-} ions were incorporated in the apatite lattice during HA/CHA formation. This assumption is based on the lower Gibbs free energy of formation of $CaCO_3$ compared to that of Na_2CO_3 from respective ions in solution. Note that there are only two cations, Ca^{2+} and Na^+, available to react with CO_3^{2-} in PBS solution during HA/CHA formation.[39] ATR-FTIR spectra of PBS-incubated samples with different nanopore sizes also suggest the presence of Type-B CHA by the position of $v_3(CO_3^{2-})$ band at 1418 cm^{-1}, as shown in Figure 4 and discussed in ATR-FTIR analysis of PBS-incubated nanoporous glass monoliths section.[33] Furthermore, the ATR-FTIR spectra indicate the absence of Type-A CHA which would have produced an absorbance peak for $v_3(CO_3^{2-})$ at 1546 cm^{-1}.[33]

Influence of nanopore size on HA/CHA formation pathway

The microstructural analysis, as described in Thickness and microstructure of PBS-incubated nanoporous glass monoliths section, reveals two distinct patterns of HA/CHA layer formation after the incubation of nanoporous glass monoliths in PBS: (a) deposition of HA/CHA only on the outermost surface of monoliths, and (b) formation of HA/CHA on the surface as well as within the nanopores below the surface. To establish the pathways that lead to these two morphologies of HA/CHA layer, we note that in pathway (a), there is negligible formation of HA/CHA inside the pores, as shown schematically in Figure 9(a). This pathway was observed on samples with 6-, 15-, or 31-nm pore size, where the cross-sectional EDS elemental maps, as depicted in Figure 6, show no overlap between Ca or P signal from the HA/CHA formation, and Si signal from the underlying glass substrate. However, if the nanopore size is sufficiently large (e.g., 44 nm), HA/CHA form also within the interconnected nanopore network, resulting in HA/CHA incorporation deep inside. Since HA/CHA deposition can take place on the surface of nanoporous monoliths regardless of nanopore size, there are two layers of HA/CHA created in pathway (b): HA/CHA surface-deposited layer and HA/CHA layer incorporated inside the nanopores, as illustrated in Figure 9(b). This pathway was observed on 44-nm samples after PBS incubation. The cross-sectional EDS elemental maps of such samples in Figure 6 show that the surface-deposited HA/CHA layer consists of only Ca and P signals indicating a "Pure HA/CHA" layer. By contrast, the HA/CHA-incorporated layer (marked as "HA/CHA + Glass") shows an overlap of Ca and P signals (from HA/CHA) with Si signal (from the underlying glass substrate), indicating that HA/CHA formed within the nanopore network.

HA/CHA formation is dependent on the presence of both Ca^{2+} and PO_4^{3-} in the solution to be present at the deposition surface. During the glass dissolution process, Ca^{2+} ions are readily supplied by ion exchange reaction at the interface between glass network and PBS shown in eq. 1.2. Thus, the availability of PO_4^{3-} ions at the forming surface controls the formation of HA/CHA there. Then the differences between the two morphologies of HA should be caused by a pore-size limited diffusion of PO_4^{3-} ions.

We may anticipate two phenomena occurring during glass dissolution and HA/CHA formation, which could restrict the diffusion of PO_4^{3-} ions and make it pore size dependent: electrostatic screening of ions and "clogging" of nanopores. The electrostatic screening is expected from the negatively charged glass surface with the formation of silanol (Si—OH) species during glass dissolution (see eq. 1.3). As pH in PBS increases during ion exchange process (eq. 1.2), Si—OH should undergo a dissociation equilibrium reaction with OH^- as follows [40]:

$$Si-OH + OH^- \rightleftharpoons Si-O^- + H_2O \qquad (4.1)$$

The layer of Si—O^- creates an electrical double layer due to the negative electric field on the surface of nanopore

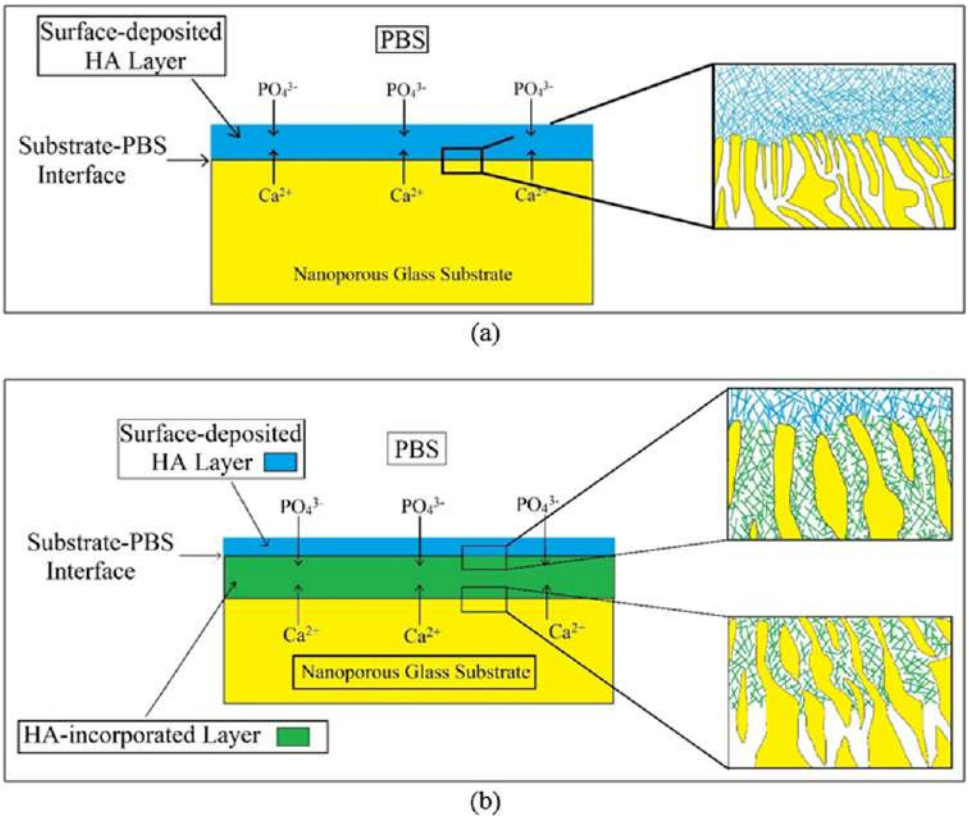

FIGURE 9. Schematic drawings of the two pathways of HA/CHA formation: (a) HA/CHA surface deposition seen on 6-, 15-, and 31-nm nanoporous samples (b) HA/CHA incorporation seen on 44-nm nanoporous samples.

walls, making the effective pore size, seen by PO_4^{3-} ions, smaller than the actual nanopore size. The expanse of the electrostatic screening can be expressed as the Debye length (λ_D) which is a measure of the distance over which electrostatic forces decay in an electrolyte solution.[41] The Debye length is inversely proportional to the square root of the ionic strength of the electrolyte solution and is written as follows[41]:

$$\lambda_D = \sqrt{\frac{\varepsilon_r k_B T}{2I}}$$

where ε_r is the relative permittivity of the electrolyte solution, k_B is the Boltzmann constant, T is the absolute temperature of the electrolyte solution, and I is the ionic strength of the electrolyte solution. For PBS solution at pH 7.4, ε_r =80 and I = 162.7 mMol.[42] The Debye screening length is approximately 1 nm. Since the ionic diameter of hydrated PO_4^{3-} in aqueous solution is only 0.678 nm,[43] the effective pore size for all the samples seen by PO_4^{3-} is still significantly larger than the size of hydrated PO_4^{3-} ions, and therefore, should not be able to prevent their diffusion into the nanopore network. Hence, the electrostatic screening effect, although cannot be ignored, does not play a major role in restricting diffusion of phosphate ions through the nanopores of glass monoliths investigated here.

The other phenomenon that can restrict the diffusion of PO_4^{-3} ions is the clogging of nanopores with the formation and growth of HA/CHA layer. We propose that chronological progression of HA/CHA formation and growth during PBS incubation for relatively small nanopore sizes occurs as shown schematically in Figure 10. Here, nanopores are quickly clogged by the initial formation and growth of HA/CHA due to their small size, allowing only HA/CHA surface deposition. Conversely, if the nanopores are sufficiently large, it would be too difficult for the growing HA/CHA layer to completely clog them. Then, it is reasonable to expect that both HA/CHA surface deposition and HA/CHA incorporation within the nanopore network will occur, as shown in Figure 11. As PBS comes in contact with the present 30C70S nanoporous glass monoliths, calcium within glass structure leaches out as Ca^{2+} ions into the solution through ion exchange process, as illustrated in Figures 10(a) and 11(a). Since PO_4^{3-} ions are readily available in PBS, the adsorption of amorphous calcium phosphate (ACP) begins on the top surface of nanopore network [Figures 10(b) and 11(b)]. HA/CHA layer is then formed via crystallization of ACP. At the early stage of HA/CHA formation, PO_4^{3-} ions can freely move into the nanopores which causes HA/CHA to grow along the "throats" of nanopores at the same rate as on the top surface, thereby narrowing the openings of nanopores [Figures 10(c) and 11(c)]).

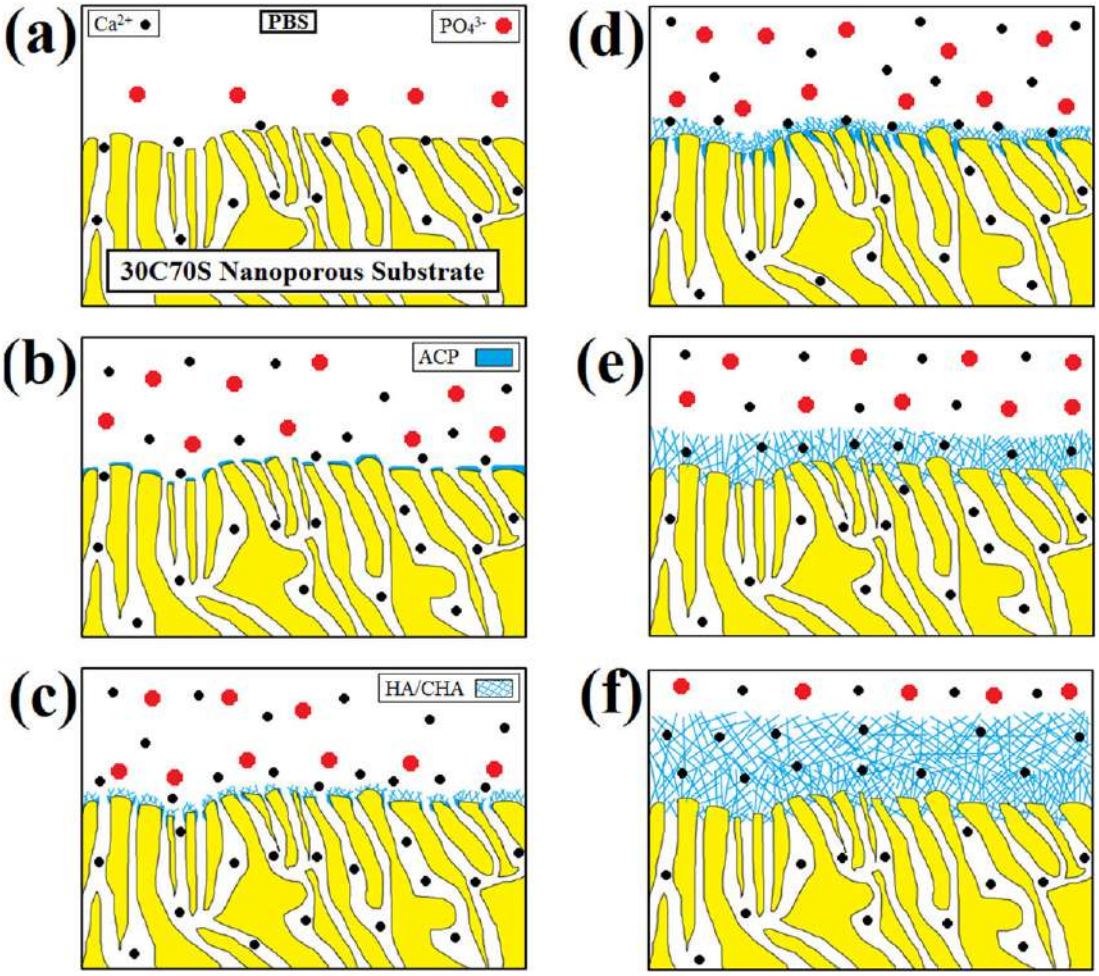

FIGURE 10. Chronological representation of HA/CHA formation and growth on relatively small nanopores as observed on HA/CHA surface deposition pathway: (a) $PO4^{3-}$ ions from PBS encounters dissolved Ca^{+2} at the top surface as PBS first comes into contact with nanoporous glass monoliths (b) amorphous calcium phosphate (ACP) begins to adsorb on the top surface of the nanoporous glass monoliths (c) HA/CHA forms via crystallization of ACP and grows along the throats of nanopores, narrowing the openings of nanopores (d) HA/CHA layer starts to fully cover the openings of nanopores (e) HA/CHA layer fully clogs the openings of nanopores, PO_4^{3-} from entering the nanopores while allowing Ca^{+2} to diffuse into PBS (f) HA/CHA continues to grow only on the top surface of the nanoporous glass monoliths after HA/CHA fully clogs the nanopore openings.

With relatively small nanopore sizes, the growth of HA/CHA layer quickly clogs the openings of nanopores, as illustrated in Figure 10(d). Although the diffusion of both Ca^{2+} and PO_4^{3-} ions is restricted by HA/CHA layer covering the openings of nanopores, the reduction in diffusivity of PO_4^{3-} ions due to HA/CHA coverage of nanopore openings can be orders of magnitude higher than that experienced by Ca^{2+} ions. This is because hydrated PO_4^{3-} ions with 0.678 nm in diameter,[43] is approximately three times larger than hydrated Ca^{2+} ions, 0.233 nm in diameter.[44] Also, PO_4^{3-} ions have a higher total free charge which can lead to higher degree of restriction by electrostatic screening effect compared to Ca^{2+} ions. Hence, Ca^{2+} ions can readily diffuse into PBS, while PO_4^{3-} ions cannot easily enter the nanopore network, causing HA/CHA to grow only on the top surface of the nanoporous monoliths after HA/CHA coverage of the nanopore openings, as illustrated in Figure 10(e,f). This is the case of HA/CHA surface deposition pathway [Figure 9 (a)], observed on 6-, 15-, and 31-nm nanoporous samples.

Conversely, with larger nanopore sizes, the growth of HA/CHA layer takes longer to fully clog the openings of nanopores compared to the case of smaller nanopore sizes, and we suspect that the larger structure of HA/CHA occupying the openings of larger nanopores has poor integrity, comprising of sufficient porosity. Such porous clogs allow the PO_4^{3-} ions to enter nanopores and form HA/CHA within the nanopore network [Figure 11(c,d)]. As previously discussed, because the diffusion of PO_4^{3-} into nanopore network is more severely hindered by HA/CHA layer compared to that of Ca^{2+}, after HA/CHA fully covers the nanopore openings, HA/CHA layer only continues to grow on the surface-deposited layer at a much faster rate than inside the pores, as depicted in Figure 11(e,f). Hence, the depth to which HA/CHA can form inside the nanoporous monoliths is governed by how quickly the nanopore openings is covered by HA/CHA layer and the integrity of such a layer. Obviously, the thickness of HA/CHA incorporation layer is ultimately dependent on the size of nanopores. This latter case is referred to as HA/CHA

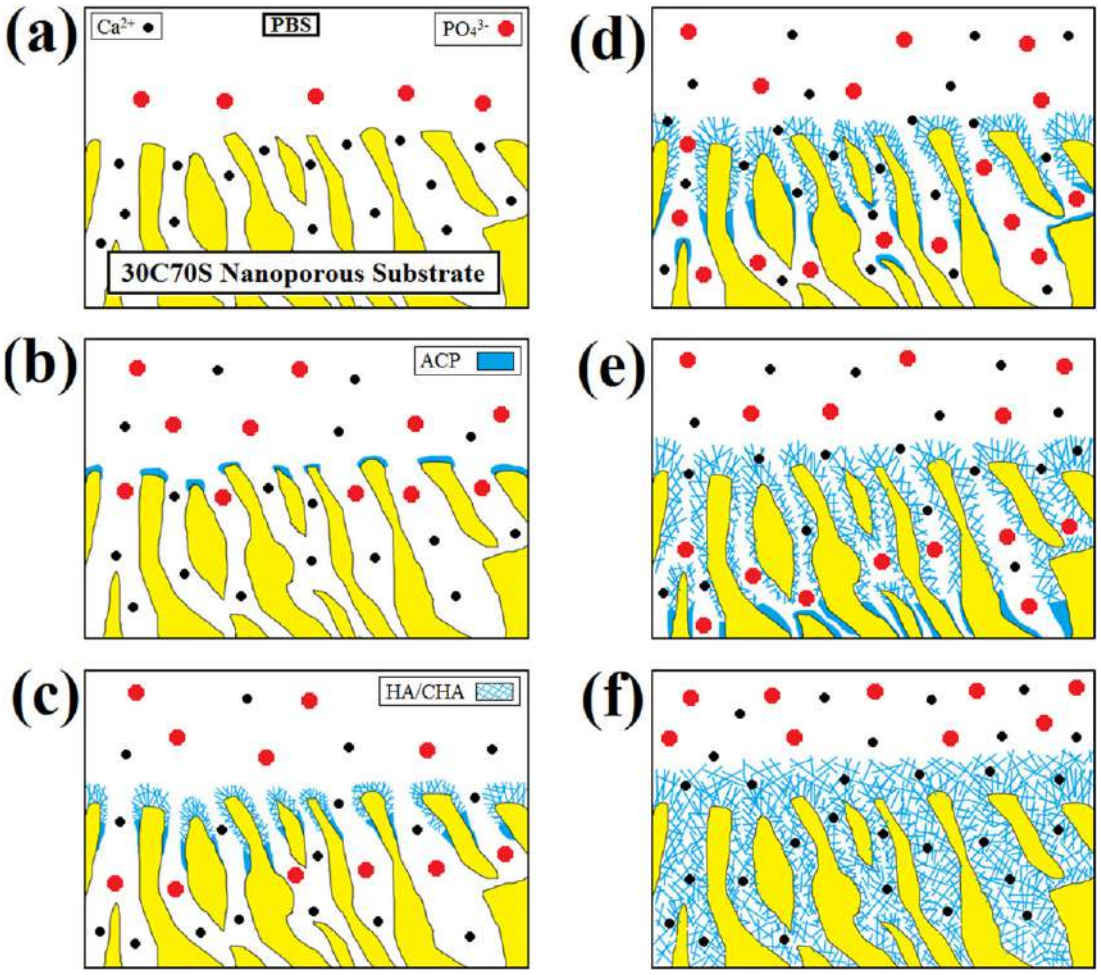

FIGURE 11. Chronological representation of HA/CHA formation and growth on relatively large nanopores as observed on HA/CHA incorporation pathway: (a) PO_4^{-3} ions from PBS encounters dissolved Ca^{+2} at the top surface as PBS first comes into contact with nanoporous glass monoliths (b) amorphous calcium phosphate (ACP) begins to adsorb on the top surface of the nanoporous glass monoliths (c) HA/CHA forms via crystallization of ACP and grows along the throats of nanopores (d) nanopore openings becomes progressively narrower as HA/CHA forms inside the nanopores (e) HA/CHA layer on the top surface begins to clog the openings of nanopores, slowing down the diffusion of PO_4^{-3} ions into the nanopores (f) HA/CHA layer fully clogs the openings of nanopores, allowing HA/CHA to continue growing only on the top surface of nanoporous glass monoliths.

incorporation pathway [Figure 9(b)], where both surface deposition and incorporation of HA/CHA were observed on 44-nm nanoporous samples. Evidently, the clogging of large pores within the 44-nm samples did not become fully effective after PBS incubation, since the HA-incorporated layer, referred as "HA/CHA + Glass" layer in Figure 6, is significantly thicker than the HA/CHA surface-deposited layer, referred to as "Pure HA/CHA" layer in Figure 6. So HA/CHA continues to grow both inside the pore and on the surface of this sample, as shown schematically in Figure 11(e). We expect that the HA/CHA incorporation will continue deeper inside the nanoporous monoliths if the PBS incubation period were to continue beyond 3 days.

The nanopore size not only determines the pathway of HA/CHA formation by restricting or permitting the transport of PO_4^{3-} ions, but also affects the transport of Ca^{2+} ions required for the HA/CHA formation. Since PO_4^{3-} ions are not able to diffuse into nanopores in the case of HA/CHA deposition pathway seen in samples with pore sizes ≤33 nm, the HA/CHA deposits only on the external surface where PO_4^{3-} ions are freely available. Then the growth rate is determined exclusively by the transport rate of Ca^{2+} through nanopores. As nanopore size increases from 6 nm to 31 nm, Ca^{2+} transport becomes less hindered, resulting in higher concentration of Ca^{2+} ions in PBS during incubation [see Figure 8(b)], faster consumption rate of PO_4^{3-} [Figure 8(c)], and thicker surface-deposited HA layer (Figure 6). Conversely, because PO_4^{-3} ions were able to diffuse into 44-nm nanopores, they readily reacted with Ca^{2+} inside the nanopores to form HA/CHA. This results in relatively lower PO_4^{3-} concentration available at the surface of nanoporous monoliths compared to other nanopore sizes, which explains why PO_4^{3-} concentration in PBS is the lowest after incubation with 44-nm samples. Furthermore, as previously mentioned, it is suspected that the 44-nm pores are not yet fully clogged after PBS incubation, so a greater number of Ca^{2+} ions leached from the bulk of the samples are able to

diffuse into PBS, resulting in the highest Ca^{2+} concentration in PBS used with 44-nm samples. Hence, despite having the largest nanopores and the highest concentration of Ca^{2+} in post-incubation PBS, 44-nm samples had the thinnest surface-deposited HA/CHA layer and the slowest HA/CHA growth rate among the four nanopore sizes, as seen in Figure 6.

HA/CHA microstructure development

An insightful observation of the present work, which is also of practical importance, is that nanopore size affects the microstructure of HA/CHA layer. In particular, as the overall growth rate of HA/CHA layer increases with change in nanopore size as discussed above, its microstructure evolves from needle-like, to plate-like, and to flower-like microstructure. At a relatively slow growth rate, needle-like microstructures were observed on 6- and 44-nm nanoporous samples with the overall growth rate of 0.5 ± 0.1 μm/day and 0.2 ± 0.1 μm/day, respectively. With higher overall growth rate of 0.7 ± 0.2 μm/day on 15-nm and 0.9 ± 0.2 μm/day on 31-nm nanoporous samples, plate-like and flower-like HA/CHA microstructure were found, respectively. The influence of growth rate on HA/CHA microstructures can be explained by the following mechanism:

At slow HA/CHA overall growth rate under nearly equilibrium condition with just enough supply of Ca^{2+} and PO_4^{3-} for HA/CHA formation, the HA/CHA crystals grow predominantly in [0001] direction (along the c-axis), with a much slower rate within the basal plane.[2,3] As a result, long hexagonal rods or needles comprising of stable (1100) planes of HA crystals are formed under near-equilibrium condition as illustrated in Figure 12(a). At intermediate overall growth rate with low supersaturation of Ca^{2+} and PO_4^{3-} supply, the growth condition of HA/CHA shifts to kinetic-limited crystal growth, where the fluctuation of Ca^{2+} and PO_4^{3-} supply favors one growth direction along a-axis over the other, leading to single-direction growth distortion in basal plane. Since the growth rate of narrow faces is higher than the larger faces due to a smaller required amount of supply per unit area, the single-direction distortion in basal plane is enhanced as HA/CHA crystals continue to grow, and plate-like microstructure is consequently formed as seen Figure 12(b). At fast overall HA/CHA growth rate with high degree of supersaturation, multiple growth directions along a-axis can be favored over few others under kinetic-controlled condition, leading to multidirection growth distortion of HA/CHA crystals in basal plane. As distorted HA/CHA crystals continue to grow with faster growth rate of narrower faces compared to larger faces, the enhanced, multi-direction distortion results in the formation of flower-like microstructure as illustrated in Figure 12(c).

CONCLUSIONS

Due to its close chemical crystallographic resemblance to natural bones, the newly formed HA layer has been shown to be critical for the biological interaction and bonding between the surfaces of bioactive glasses and osteoblast (bone) cells. Recent studies suggest that the presence of nanopores significantly improves the performance of bioactive glass under in vitro as well as in vivo conditions. Here, we report the influence of nanopore size alone (i.e., keeping specific surface are fixed) on the pathway, growth rate, and microstructure of HA/CHA layer formed on $30CaO—70SiO_2$ model bioactive glass when incubated in PBS. Glass monoliths of very similar specific surface area but different nanopore sizes were fabricated by combining conventional sol–gel process with hydrothermal solvent exchange and sintering to exclude the surface area effects on HA/CHA formation.

The results show a complex influence of nanopore size ranging from 6 nm to 44 nm on the morphology, growth rate, and microstructure of HA/CHA layer that mostly comprises of Type-B CHA (i.e., $Ca_{10}(PO_4)_2(CO_3)_6(OH)_2$). Due to pore-size dependent diffusion of PO_4^{3-} ions, two HA/CHA formation pathways were observed: plain deposition only on the surface, and formation of HA/CHA within the nanopores together with surface deposition. The thickness of HA/CHA layer formed on the surface of a nanoporous glass monolith is determined by the pore-size limited transport of Ca^{2+} ions that leach out via ion-exchange from nanoporous glass substrates. Furthermore,

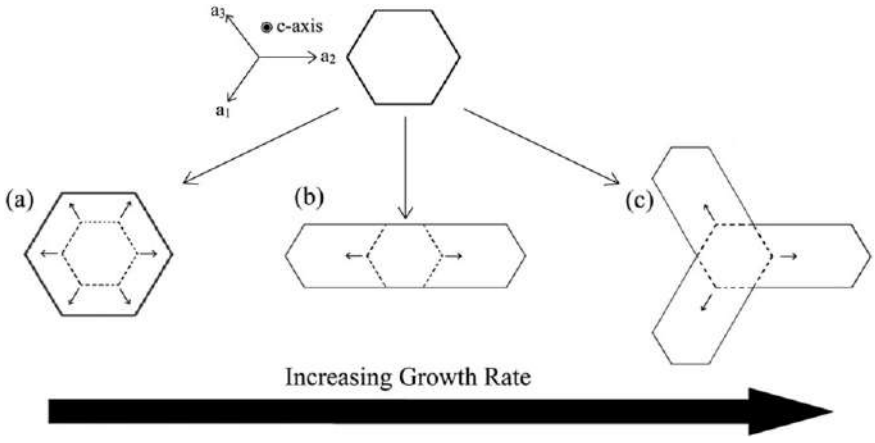

FIGURE 12. Schematic illustrations of the influence of HA/CHA growth rate on its microstructures: (a) equal growth rate in all directions in basal plane under equilibrium condition at slow overall HA/CHA growth rate, resulting in needle-like microstructure (b) single-direction growth distortion in basal plane under kineticcontrolled condition at intermediate HA/CHA overall growth rate, resulting in plate-like microstructure (c) multidirection growth distortion in basal plane under kinetic-controlled condition at fast HA/CHA overall growth rate, resulting in flower-like microstructure.

with rising overall growth rate controlled by nanopore size, HA/CHA microstructures evolve from needle-like to plate-like to flower-like appearance, respectively.

ACKNOWLEDGMENTS

They also thank Professor Dmitri Vezenov for helpful comments. The authors declared no potential conflicts of interest with respect to the research, authorship, and/or publication of this article.

REFERENCES

1. Jones JR. Review of bioactive glass: From Hench to hybrids. Acta Biomater 2013;9(1):4457–4486.
2. Vallet-Regí M, González-Calbet JM. Calcium phosphates as substitution of bone tissues. Prog Solid State Chem 2004;32(1):1–31.
3. Mucalo MR. Hydroxyapatite (HAp) for Biomedical Applications, 1st ed. United Kingdom: Woodhead Publishing; 2015.
4. Hutmacher DM, Schantz JT, Lam CS, Tan KC, Lim TC. State of the art and future directions of scaffold-based bone engineering from a biomaterials perspective. J Tissue Eng Regen Med 2007;1(4):245–260.
5. Hench LL, Splinter RJ, Allen WC, Greenless TK. Bonding mechanisms at the interface of ceramic prosthetic materials. J Biomed Mater Res 1971;5(6):117–141.
6. Xynos ID, Edgar AJ, Buttery LD, Hench LL, Polak JM. Ionic products of bioactive glass dissolution increase proliferation of human osteoblasts and induce insulin-like growth factor II mRNA expression and protein synthesis. Biochem Biophys Res Commun 2000;276(2):461–465.
7. Xynos ID, Edgar AJ, Buttery LD, Hench LL, Polak JM. Gene-expression profiling of human osteoblasts following treatment with the ionic products of bioglass 45S5 dissolution. J Biomed Mater Res 2001;55(2):151–157.
8. Hench LL. Bioceramics: From concept to clinic. J Am Ceram Soc 1991;74(7):1487–1510.
9. Sepulveda P, Jones JR, Hench LL. In vitro dissolution of melt-derived 45S5 and sol-gel derived 58S bioactive glasses. J Biomed Mater Res 2002;61(2):301–311.
10. Woo KM, Chen VJ, Ma PX. Nano-fibrous scaffolding architecture selectively enhances protein adsorption contributing to cell attachment. J Biomed Mater Res A 2003;67(2):531–537.
11. Peltola T, Jokinen M, Rahiala H, Levanen E, Rosenholm JB, Kangasniemi I, Yli-Urpo A. Calcium phosphate formation on porous sol-gel-derived SiO_2 and CaO-P_2O_5-SiO_2 substrates in vitro. J Biomed Mater Res 1999;44(1):12–21.
12. Wang S, Falk MM, Rashad A, Saad MM, Marques AC, Almeida RM, Marei MK, Jain H. Evaluation of 3D nano-macro porous bioactive glass scaffold for hard tissue engineering. J Mater Sci Mater Med 2011;22(5):1195–1203.
13. Wang S, Kowal TJ, Marei MK, Falk MM, Jain H. Nanoporosity significantly enhances the biological performance of engineered glass tissue scaffolds. Tissue Eng A 2013;19(13–14):1632–1640.
14. Marques AC, Jain H, Almeida RM. Sol-gel derived nano/macroporous scaffolds. Phys Chem Glasses Eur J Glass Sci Technol B 2007; 48(2):65–68.
15. Swift P. Adventitious carbon - the panacea for energy referencing. Surf Interface Anal 1982;4(2):47–51.
16. Beamson G, Briggs D. High resolution XPS of organic polymers: The Scienta ESCA300 database. J Chem Edu 1993;70(1):A25.
17. Santos JD, Jha LJ, Monteiro FJ. In vitro calcium phosphate formation on SiO_2-Na_2O-CaO-P_2O_5 glass reinforced hydroxyapatite composite: A study by XPS analysis. J Mater Sci Mater Med 1996;7(3):181–185.
18. Lo PH, Tsai WT, Lee JT, Hung MP. The electrochemical behavior of electroless plated Ni-P alloys in concentrated NaOH solution. J Electrochem Soc 1995;142(1):91–96.
19. Nefedov VI, Salyn YV, Leonhardt G, Scheibe R. A comparison of different spectrometers and charge corrections used in X-ray photoelectron spectroscopy. J Electron Spectros Relat Phenomena 1977; 10(2):121–124.
20. Wren AG, Phillips RW, Tolentino LU. Surface reactions of chlorine molecules and atoms with water and sulfuric acid at low temperatures. J Colloid Interface Sci 1979;70(3):544–557.
21. Dean JA, Lange NA. Lange's Handbook of Chemistry, Vol.15. New York, NY: McGraw-Hill; 1999 Ch. 6.
22. Landis WJ, Martin JR. X-ray photoelectron spectroscopy applied to gold-decorated mineral standards of biological interest. J Vac Sci Technol 1984;2:1108–1111.
23. Lafon JP, Champion E, Bernache-Assollant D. Processing of AB-type carbonated hydroxyapatite $Ca_{10-x}(PO_4)_{6-x}(CO_3)_x(OH)_{2-x-2y}(CO_3)_y$ ceramics with controlled composition. J Eur Ceram Soc 2008;28(1):139–147.
24. Gibson IR, Bonfield W. Novel synthesis and characterization of an AB-type carbonate-substituted hydroxyapatite. J Biomed Mater Res 2002;59(4):697–708.
25. Chafik El Idrissi B, Yamni K, Yacoubi A, Massit A. A novel method to synthesize nanocrystalline hydroxyapatite: Characterization with X-ray diffraction and infrared spectroscopy. IOSR J Appl Chem 2014;7(5):107–112.
26. Tkalcec E, Sauer M, Nonninger R, Schmidt H. Sol-gel-derived hydroxyapatite powders and coatings. J Mater Sci 2001;36(21): 5253–5263.
27. Wagner CD, Muilenberg GE. Handbook of X-Ray Photoelectron Spectroscopy: A Reference Book of Standard Data for Use in x-Ray Photoelectron Spectroscopy. Eden Prairie, MN: Perkin-Elmer Corporation; 1979.
28. Raynaud S, Champion E, Bernache-Assollant D, Thomas P. Calcium phosphate apatites with variable Ca/P atomic ratio I. Synthesis, characterisation and thermal stability of powders. Biomaterials 2002;23(4):1065–1072.
29. Yazdi AFA, Yazdani A, Khozani TT, Kalantar M. Extraction and viability checking of various carbonated hydroxyapatite by Wharton's jelly mesenchymal stem cell. Sci Int 2013;1(5):132–138.
30. Berzina-Cimdina L, Borodajenko N. Research of calcium phosphates using Fourier transform infrared spectroscopy, Book 6 of "Infrared Spectroscopy—Materials Science, Engineering and Technology".Croatia: Theophile Theophanides, InTech; 2012.
31. Fleet ME. Infrared spectra of carbonate apatites: $\nu 2$-region bands. Biomaterials 2009;30(8):1473–1481.
32. Elliott JC. Structure and chemistry of the apatites and other calcium orthophosphates, Book 18 of "Studies in Inorganic Chemistry". Amsterdam, Netherlands: Elsevier Science; 2013.
33. Xu G, Aksay IA, Groves JT. Continuous crystalline carbonate apatite thin Films. A biomimetic approach. J Am Chem Soc 2001;123(10): 2196–2203.
34. Poralan GM Jr, Gambe JE, Alcantara EM, Vequizo RM. X-ray diffraction and infrared spectroscopy analyses on the crystallinity of engineered biological hydroxyapatite for medical application. IOP Conf Ser Mater Sci Eng 2015;79:012028.
35. Kabekkodu S. 2016 JCPDS International Centre of Diffraction Data. Newton Square, PA: International Centre for Diffraction Data; 1980.
36. Xue C, Chen Y, Huang Y, Zhu P. Hydrothermal synthesis and biocompatibility study of highly crystalline carbonated hydroxyapatite nanorods. Nanoscale Res Lett 2015;10(1):1018–1023.
37. Danilchenko SN, Kukharenko OG, Moseke C, Protsenko IY, Sukhodub LF, Sulkio-Cleff B. Determination of the bone mineral crystallite size and lattice strain from diffraction line broadening. Cryst Res Technol 2002;37(11):1234–1240.
38. Rusu VM, Ng CH, Wilke M, Tiersch B, Fratzl P, Peter MG. Size-controlled hydroxyapatite nanoparticles as self-organized organic–inorganic composite materials. Biomaterials 2005;26(26): 5414–5426.
39. Linstrom PJ, Mallard WG. NIST Chemistry WebBook - Standard Reference Database Number 69. Gaithersburg, MD: National Institute of Standards and Technology; 2005.
40. Behrens SH, Grier DG. The charge of glass and silica surfaces. J Chem Phys 2001;115(14):6716–6721.
41. Israelachvili JN. Intermolecular and Surface Forces. Waltham, MA: Academic Press; 2011.
42. Mousavi MP, Bühlmann P. Reference electrodes with salt bridges contained in nanoporous glass: An underappreciated source of error. Anal Chem 2013;85(19):8895–8901.
43. Kiriukhin MY, Collins KD. Dynamic hydration numbers for biologically important ions. Biophys Chem 2002;99(2):155–168.
44. Marcus Y. Ionic radii in aqueous solutions. Chem Rev 1988;88(8): 1475–1498.